Optimization of the Oxidation Behavior and Mechanical Properties by Designing the TiB$_2$/ZrO$_2$ Multilayers

Dong Mao [1,2], Yang Xu [1,2], Lei Dong [1,2,*], Jie Wu [1,2], Mengli Zhao [1,2] and Dejun Li [1,2,*]

[1] College of Physics and Materials Science, Tianjin Normal University, Tianjin 300387, China; guozheng@tjnu.edu.cn (D.M.); ldong@tjnu.edu.cn (Y.X.); jiewu@tjnu.edu.cn (J.W.); zml0506@tjnu.edu.cn (M.Z.)

[2] Tianjin International Joint Research Center of Surface Technology for Energy Storage Materials, Tianjin Normal University, Tianjin 300387, China

* Correspondence: dlei0008@tjnu.edu.cn (L.D.); dejunli@tjnu.edu.cn (D.L.); Tel.: +86-22-2376-6519 (D.L.)

check for updates

Abstract: TiB$_2$/ZrO$_2$ multilayers with different modulation ratios (at a fixed modulation period of 50 nm) ranging from 2:1 to 6:1 were deposited by magnetron sputtering. The oxidation behavior of the as-deposited multilayers was investigated at 600 °C in air. The microstructures, mechanical properties, and oxidation resistance of the multilayers were analyzed and compared. The results indicate that discontinuous oxidation retarded the inward diffusion of oxygen and the outward diffusion of metallic components. The formation of dense (Ti, B)-oxide scale and internally inserted ZrO$_2$ layers in the TiB$_2$/ZrO$_2$ multilayers enhanced the oxidation resistance. Moreover, the oxidation resistance of the multilayers increased as modulation ratio decreased. The hardness and elastic modulus of the TiB$_2$/ZrO$_2$ multilayers were maximized (23.9 and 303.1 GPa, respectively) at the modulation ratio of 6:1. After annealing, the formation of thick ZrO$_2$ layers did not lead to sustained increases in hardness. The maximum hardness and elastic modulus were obtained at the critical modulation ratio of 4:1, and good adhesion strength with the substrate was also observed. The oxidation mechanism and experimental results demonstrate that controlling the modulation ratio of multilayers can produce synergetic enhancements in the oxidation resistance and mechanical properties of multilayers after high-temperature oxidation.

Keywords: TiB$_2$/ZrO$_2$ multilayers; modulation ratio; oxidation resistance; mechanical properties

1. Introduction

The development of industry has generated increased demand for coatings with outstanding mechanical properties and oxidation resistance at high temperature for use in cutting tools and microelectronics [1,2]. TiB$_2$ coatings have been widely used due to their high melting point, high hardness, good wear resistance, excellent corrosion resistance, and good thermal conductivity. However, transition metal boride ceramics, which belong to the class of non-oxide coatings, are prone to oxidation, especially at high temperature, which limits their application at high temperatures [3–6]. Considering the harsh environments to which protective coatings are exposed, it is particularly important to improve their oxidation resistance as a protective function. The incorporation of other materials might modify the microstructure of TiB$_2$ to further improve oxidation resistance. As an incorporated material, ZrO$_2$ was chosen in this study, because it has widespread applications in thermal barrier coatings due to its low thermal conductivity and high thermal stability [7–11].

Many surface modification techniques such as thermal spraying [12], laser cladding [13], ion implantation [14], and double-glow plasma surface alloying [15], have been adopted to enhance the

high-temperature oxidation resistance of substrates. These methods can improve the thermal oxidation resistance of substrates to some extent. However, they suffer various drawbacks, such as poor adhesion, large thermally affected zones, complex processing steps, and high cost, which limit their application. Magnetron sputtering possesses the advantages of preparing dense and uniform coatings with strong adhesion to the substrate. The composition and microstructure of the coating can be controlled by adjusting the sputtering parameters [16,17]. Multilayers prepared by magnetron sputtering not only combine the advantages of the different constituent materials but also have better performance and microstructure compared to single layers of their respective components due to the superhardness effect, quantum effects, and macro-tunneling effects between the nanolayers [18–22]. In addition to resulting in excellent mechanical properties, the formation of multilayer structures can also improve the oxidation resistance at high temperatures through limited intermixing [23–25]. TiB_2 has a higher hardness (~34.0 GPa) than ZrO_2 (~11.8 GPa), and can thus effectively improve the mechanical properties of multilayers. Inserting ZrO_2 layers can also solve the problem of poor high-temperature oxidation resistance that afflicts boride coatings intended to withstand high-speed cutting tools. Unlike the small modulation periods used in past studies, a larger modulation period (50 nm) is expected to maximize the performances of the two component materials, resulting in outstanding mechanical properties and oxidation resistance.

In this study, TiB_2 and ZrO_2 monolayers and TiB_2/ZrO_2 multilayers with the same modulation periods (50 nm) and various modulation ratios ($t_{TiB_2}:t_{ZrO_2}$ = 2:1 to 6:1) were synthesized on silicon wafer substrates via magnetron sputtering. The high-temperature oxidation resistance of the samples was studied by thermogravimetric analysis at 600 °C in air and the effects of structural variation on the multilayer properties were evaluated. Finally, the relationships between microstructural features, chemical components, oxidation resistance, and mechanical performance were established in order to aid practical applications of multilayers in machining.

2. Experimental Details

TiB_2/ZrO_2 multilayers along with TiB_2 and ZrO_2 monolayers were prepared using an FJL560CI2 magnetron sputtering system (SKY, Shenyang, China). The high-purity (99%) TiB_2 and ZrO_2 targets were controlled by three radio-frequency (RF) cathodes. When the base pressure of the system was less than 3×10^{-4} Pa, high-purity Ar gas (99.999%) at a pressure of 0.5 Pa was introduced into the chamber. Multilayers were deposited by rotating the sample holder, alternately exposing the substrates to the TiB_2 and ZrO_2 targets. The RF modes were 120 and 80 W with a constant substrate bias of −40 V and a working pressure of 0.5 Pa. The modulation period of each sample was 50 nm, which was corresponded to 20 cycles, after which the top layers of all samples were TiB_2. By changing the sputtering time of the TiB_2 and ZrO_2 targets, thereby changing the thicknesses of the TiB_2 and ZrO_2 layers, a series of TiB_2/ZrO_2 multilayers with different modulation ratios ($t_{TiB_2}:t_{ZrO_2}$ = 2:1, 3:1, 4:1, 5:1, and 6:1) was obtained. Total thickness of the multilayers was around 900–1000 nm.

Sample crystallinity was analyzed by X-ray diffraction (XRD, D8A, Bruker, Germany) using a D/MAX 2500 diffractometer operated with Cu Kα radiation at 1.54056 Å in the range of 20°–80°. The step size and dwell time of θ–2θ were 0.02° and 7.76 s, respectively. Confocal Raman spectrometry (Horiba Jobin Yvon, LabRAM HR800, 17 mW, 514 nm, He-Ne laser, France) was used to determine the multilayer phase. Sample morphology was observed by scanning electron microscopy (SEM, TDCLS-8010, Hitachi, Japan) and transmission electron microscopy (TEM, JEOL JEM-3000F, Tokyo, Japan). The operation voltage of TEM is 300 KV. The hardness and elastic modulus of the multilayers were measured using a Nano Indenter system (STEP6, Anton Paar, Graz, Austria). The maximum indention depth for all samples was kept at 15% of the coating thickness to minimize the substrate effects. This system was also used to perform nano-scratch tests. The residual stress (σ) of the multilayers was calculated by the Stoney formula [26]: $\sigma = \frac{E_s t_s^2}{6 t_c (1-v_s) R}$, in which E_s, t_s and v_s are elastic modulus (165.6 GPa), thickness (0.4 mm) and Poisson's ratio (0.18) of the substrate respectively; t_c is the multilayer thickness; R is the radius of the curvature of the multilayer coated on substrate,

which was determined by the multilayer curvature using a surface profilometer (Ambios XP-2, Ambios Technology, California, USA). The oxidation process was conducted in air inside a chamber furnace at 600 °C for 1 h. The oxidation weight gain of the samples was measured using an electronic analytical balance (XSE, Mettler Toledo, Columbus, OH, USA) with an accuracy of 10^{-8} kg.

3. Results and Discussion

3.1. Microstructure and Crystallographic Characterization before and after Annealing in Air

Figure 1a shows the XRD patterns of the TiB_2 and ZrO_2 monolayers along with the TiB_2/ZrO_2 multilayers with different $t_{TiB_2}:t_{ZrO_2}$ before annealing. The TiB_2 layer presented a weak (100) and (101) texture of h-TiB_2, and the ZrO_2 layer existed ($\bar{1}$11) preferred orientation. In all multilayers, the main diffraction peaks indicate a hexagonal phase of TiB_2 and a monoclinic phase of ZrO_2 (m-ZrO_2). The peaks in the XRD spectra of the multilayers correspond to the (100) and (101) planes of TiB_2 and the ($\bar{1}$11) and (020) planes of m-ZrO_2. Among the TiB_2/ZrO_2 multilayers, the peak intensity was lowest for $t_{TiB_2}:t_{ZrO_2}$ = 4:1. Due to the nucleation mechanism was satisfied, the grain growth was controlled by mutual inhibition during the growth process, which also conformed to the principle that the surface energy tends to the minimum [27].
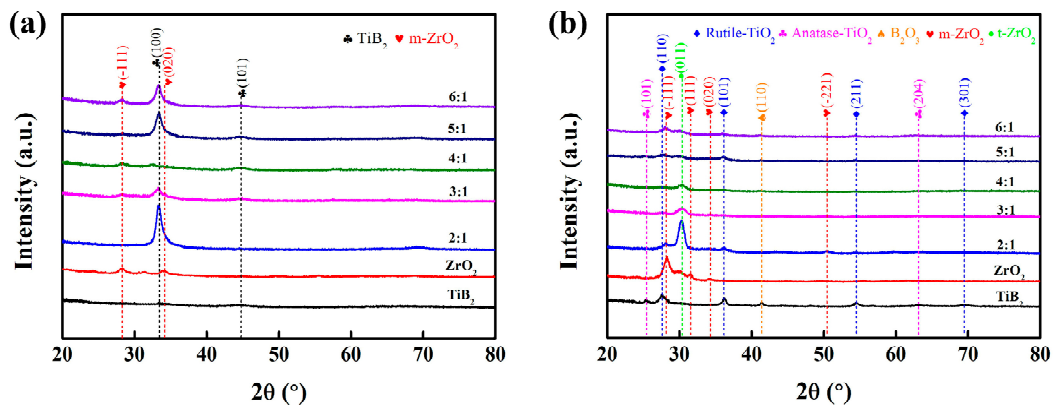

Figure 1. The XRD patterns of the TiB_2 and ZrO_2 monolayers along with the TiB_2/ZrO_2 multilayers with different $t_{TiB_2}:t_{ZrO_2}$ before (**a**) and after annealing at 600 °C for 1 h (**b**).

Figure 1b shows the XRD patterns of all samples after oxidation. For the TiB_2 monolayer, the main phases indicated in the XRD pattern are anatase TiO_2 (JCPDF#21-1272) and rutile TiO_2 (JCPDF#21-1276). For the ZrO_2 monolayer, the main phases are m-ZrO_2 (JCPDF#37-1484) and tetragonal ZrO_2 (t-ZrO_2) (JCPDF#50-1089). Only TiO_2, m-ZrO_2 and t-ZrO_2 appear in the TiB_2/ZrO_2 multilayers irrespective of the value of $t_{TiB_2}:t_{ZrO_2}$, while no TiB_2 is detected. This could suggest severe oxidation of the TiB_2 layers in the multilayers. The nucleation mechanism also was applied to oxidized films, the TiB_2/ZrO_2 multilayer with $t_{TiB_2}:t_{ZrO_2}$ = 4:1 had the lowest peak intensity. Meanwhile, the intensities of t-ZrO_2 increased and those of m-ZrO_2 decreased in the multilayer spectra, which means that oxidation promotes the growth of the high-temperature tetragonal phase of ZrO_2 grains.

Figure 2 shows the surface and cross-sectional SEM images of the TiB_2 monolayers and TiB_2/ZrO_2 multilayers ($t_{TiB_2}:t_{ZrO_2}$ = 2:1, 4:1, and 6:1) on Si substrates after annealing in air at 600°C for 1 h. The TiB_2 monolayer showed large pompon-like (Ti, B)-oxides (Figure 2a). The surface SEM images of the TiB_2/ZrO_2 multilayers were similar for all values of $t_{TiB_2}:t_{ZrO_2}$ (Figure 2b–d). All samples displayed sphere-like oxide microstructures. As $t_{TiB_2}:t_{ZrO_2}$ increased, oxygen diffused toward the inner regions of the TiB_2/ZrO_2 multilayers, leading to the formation of porous scaly deposit of (Ti, B)-oxide. The cross-sectional SEM images of the TiB_2/ZrO_2 multilayers indicate that the compact (Ti, B)-oxide scale became thicker as $t_{TiB_2}:t_{ZrO_2}$ increased. The ZrO_2 layers were thinner in the TiB_2/ZrO_2 multilayers with $t_{TiB_2}:t_{ZrO_2}$ = 6:1 compared to those with $t_{TiB_2}:t_{ZrO_2}$ = 2:1 and 4:1, resulting in decreased oxidation resistance at $t_{TiB_2}:t_{ZrO_2}$ = 6:1. That is, while the TiB_2/ZrO_2 multilayers are in their initial oxidation state,

the thick ZrO_2 layers effectively delayed the inward diffusion of oxygen and impeded the outward diffusion of metal atoms (Figure 2f–h). In contrast, the TiB_2 monolayer was almost completely oxidized, as shown in Figure 2e. The multilayered architecture clearly resulted in the compression of crystal grains and hindered grain growth, leading to the formation of a dense oxide layer that suppressed further oxidation. Moreover, ZrO_2 blocked the progress of the oxidation layer by layer, improving the overall oxidation resistance of the multilayer.
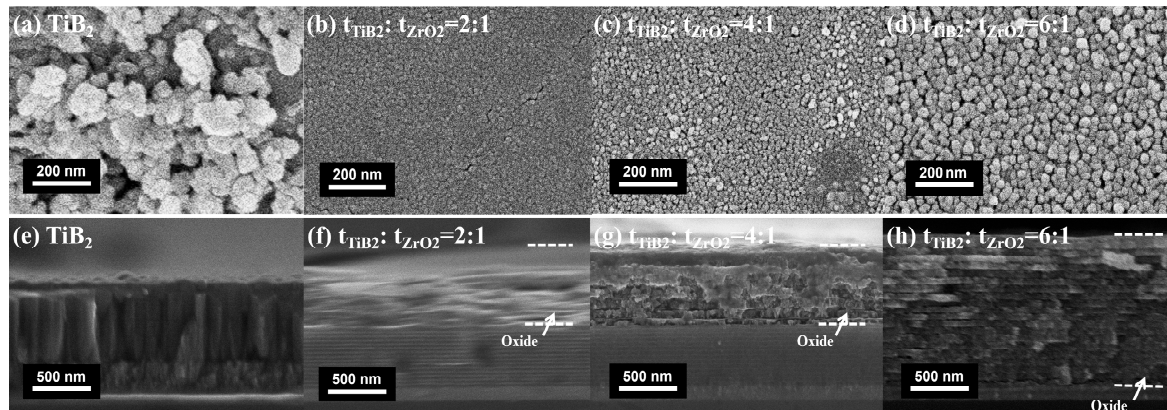

Figure 2. The surface and cross-sectional SEM images of the TiB_2 monolayers (**a**,**e**), and TiB_2/ZrO_2 multilayers with t_{TiB_2}:t_{ZrO_2} = 2:1 (**b**,**f**), t_{TiB_2}:t_{ZrO_2} = 4:1 (**c**,**g**) and t_{TiB_2}:t_{ZrO_2} = 6:1 (**d**,**h**) after annealing in air at 600 °C for 1 h.

Figure 3 shows cross-sectional high-resolution TEM (HRTEM) images and the corresponding selected-area electron diffraction (SAED) patterns of TiB_2/ZrO_2 multilayers with t_{TiB_2}:t_{ZrO_2} = 4:1 before and after annealing at 600 °C for 1 h. Both pre- and post-annealing, the images exhibited a clearly periodic multilayered structure. The diffraction rings in the inset SAED pattern of Figure 3a are characteristic of the (101) and ($\bar{1}$11) planes and can be indexed to the hexagonal structure of TiB_2 and the monoclinic structure of ZrO_2. The diffraction rings in the SAED pattern in Figure 3b correspond to the ($\bar{1}$11), and (011), and (110), (012), (211) planes and can be indexed to the monoclinic and tetragonal structures of ZrO_2 along with the rutile structure of TiO_2. These results are consistent with the qualitative information provided by XRD. The HRTEM micrographs show the well-formed crystal state of the multilayers before and after annealing. The modulation period (Λ) of the multilayers showed an appreciable increase after annealing due to the increase in grain size and the difference in molar volumes between the oxidation products. For example, the modulation periods estimated from the TEM images at the same position before and after annealing were approximately 49.6 and 52.1 nm, respectively. The single-layer thicknesses of the TiB_2, (Ti, B)-oxide, and ZrO_2 layers were approximately 39.7, 42.8, and 9 nm, respectively. In summary, the barriers formed by the ZrO_2 layers effectively blocked oxygen from entering during oxidation, helping maintain the multilayered structure. The generation of the high-temperature tetragonal phase of ZrO_2 after oxidation, as demonstrated by the SAED pattern in Figure 3b, was also favorable for the oxidation resistance of the multilayers.

The Raman spectra of the multilayers after annealing for different times at 600 °C in air are shown in Figure 4. After 30 min of oxidation (Figure 4a), peaks corresponding to ZrO_2 (315 cm^{-1}), TiO_2 (445 and 515 cm^{-1}), and TiB_2 (590 cm^{-1}) along with weak peaks of B_2O_3 (1120, 1120, and 1420 cm^{-1}) appeared in the multilayer spectrum. When the oxidation time increased to 60 min (Figure 4b), the intensities of the TiO_2 peaks at 445 and 515 cm^{-1} increased, while that of the TiB_2 peak decreased, and TiO_2 peaks appeared at 395, 638, and 826 cm^{-1} [28–31]. After annealing for 90 min (Figure 4c), the intensities of the TiO_2 and B_2O_3 peaks increased, and the TiB_2 peak disappeared. Compared to the TiB_2/ZrO_2 multilayers (Figure 4d), the intensities of the TiO_2 and B_2O_3 peaks were much higher for the TiB_2 monolayers after 60 min of oxidization, indicating that surface oxidation was more serious in the TiB_2 monolayers.
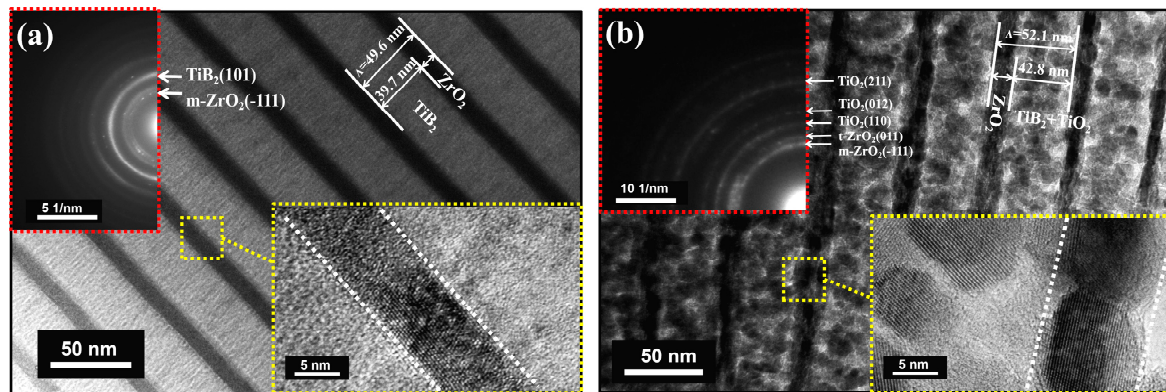
Figure 3. Cross-sectional HRTEM images and the corresponding SAED patterns of TiB_2/ZrO_2 (t_{TiB_2}:t_{ZrO_2} = 4:1) multilayers before (**a**) and after annealing at 600 °C for 1 h (**b**).
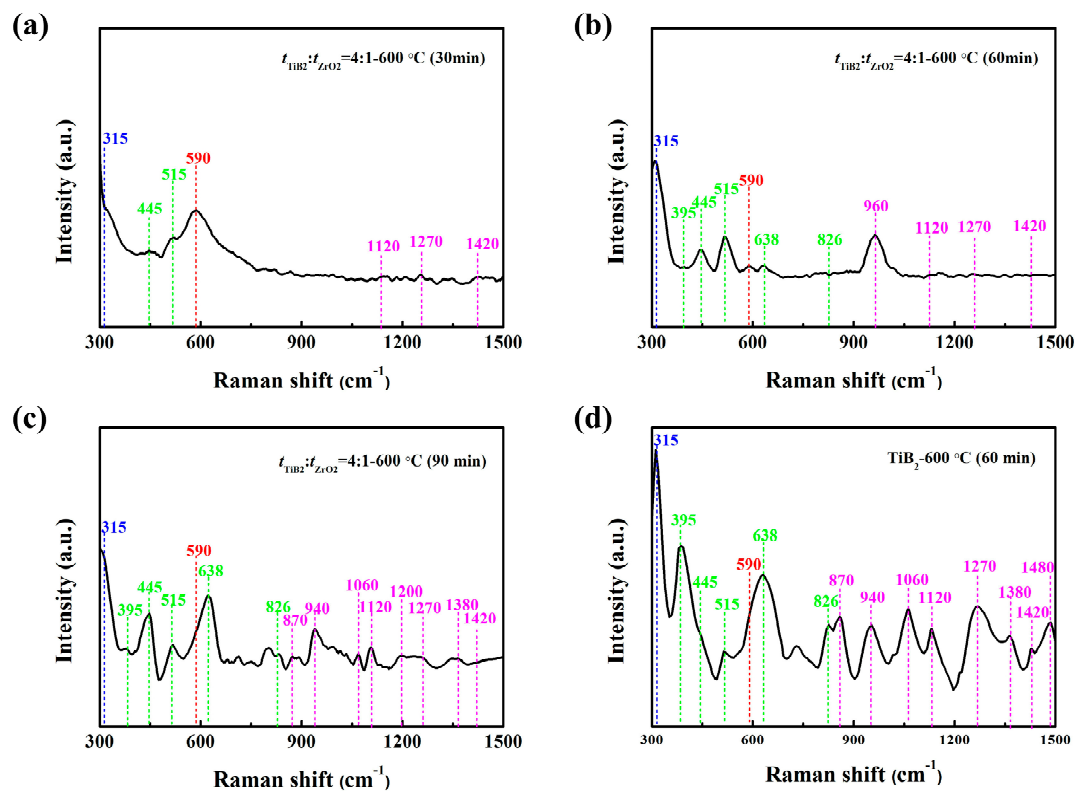

Figure 4. The Raman spectra of the TiB_2/ZrO_2 (t_{TiB_2}:t_{ZrO_2} = 4:1) multilayers after annealing for (**a**) 30 min, (**b**) 60 min, (**c**) 90 min, and TiB_2 monolayers after 60 min of oxidization (**d**).

3.2. Mechanism of Improved Oxidation Resistance and Mechanical Properties

Based on the XRD, SEM, TEM, and Raman results, high-temperature oxidation led to changes in the structure and composition of the TiB_2/ZrO_2 multilayers. To clarify the effects of high-temperature oxidation on the multilayer properties, the oxidation mechanism is depicted in Figure 5. The TiB_2/ZrO_2 multilayers were oxidized to form TiO_2 and B_2O_3 on the surfaces of the multilayers. As the oxidation time increased, the oxide content gradually increased. The primary oxidation reaction can be written as follows [32].
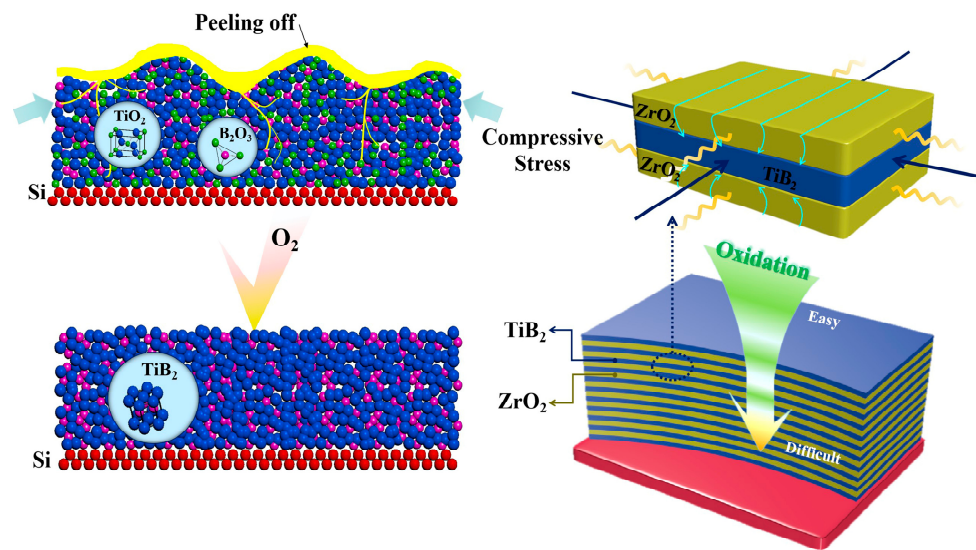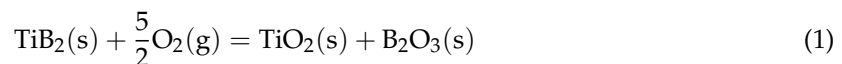
Figure 5. The oxidation mechanism of TiB$_2$ monolayer and TiB$_2$/ZrO$_2$ multilayer.

$$\mathrm{TiB_2(s)} + \frac{5}{2}\mathrm{O_2(g)} = \mathrm{TiO_2(s)} + \mathrm{B_2O_3(s)} \tag{1}$$

According to thermodynamic calculation, the standard Gibbs free energy of the reaction in Equation (1) is negative at 600 °C, indicating that the formation of TiO$_2$ and B$_2$O$_3$ phases is feasible. In the TiB$_2$ monolayer, the oxygen atoms entering the monolayer through the inter-crystal gaps can react with TiB$_2$ to form TiO$_2$ and B$_2$O$_3$, releasing the residual stress in the monolayer. The TiB$_2$ monolayer expands after annealing due to the different molar volumes of TiB$_2$ (15.5 cm^3/mol), TiO$_2$ (18.8 cm^3/mol), and B$_2$O$_3$ (38.7 cm^3/mol), and then strip from the substrate. In addition, due to the difference in the thermal expansion coefficient between the TiB$_2$ monolayer and the substrate, circular blisters form as a result of the biaxial compressive stress generated during heating. Once cracks form at the edges of the blisters, circular peeling occurs [33]. In the multilayers, the formation of circular blisters in the TiB$_2$ phase is obstructed due to the presence of internal interfaces. For ZrO$_2$, its thermal conductivity varies widely and almost continuously throughout the sample, so the ZrO$_2$ layers are hardly oxidized at all. Therefore, they form barriers hindering the oxidation process. This discontinuous oxidation of the multilayers is key to improving their oxidation resistance. Meanwhile, ZrO$_2$ has an elastic modulus of approximately 50 GPa and can form an alternating soft and hard multilayer system with TiB$_2$ [34,35]. The plastic deformation of the ZrO$_2$ layers allows the partial relief of residual stress generated by the volumetric expansion of the TiB$_2$ layers upon oxidation [1]. This mechanism contributes to the observed increase in hardness with increasing ZrO$_2$ layer thickness because the development of compressive stress in the ZrO$_2$ layers can accommodate the volume increase of the TiB$_2$ layers during oxidation.

Further experiments were carried out to verify the above oxidation mechanism. Figure 6a shows the thermogravimetric curves of the TiB$_2$ and ZrO$_2$ monolayers and the TiB$_2$/ZrO$_2$ multilayers during oxidation. Here, mass gain was defined as the mass change of the specimen per unit area corresponding to the as-deposited multilayers after annealing. After oxidation at 600 °C, the TiB$_2$ monolayers exhibited an obvious mass gain, while the ZrO$_2$ monolayers hardly gained any mass. With increasing modulation ratio, the mass gain of the TiB$_2$/ZrO$_2$ multilayers also increased. For all multilayers, the mass gain during oxidation was lower than that of the TiB$_2$ monolayer, indicating that the multilayered structure of the TiB$_2$/ZrO$_2$ multilayers is favorable for improving oxidation resistance. The TiB$_2$ and ZrO$_2$ monolayers along with the TiB$_2$/ZrO$_2$ multilayers exhibited parabolic mass gains during oxidation, indicating that the oxidation rate of the TiB$_2$/ZrO$_2$ multilayers follows a diffusion-controlled law [36,37].
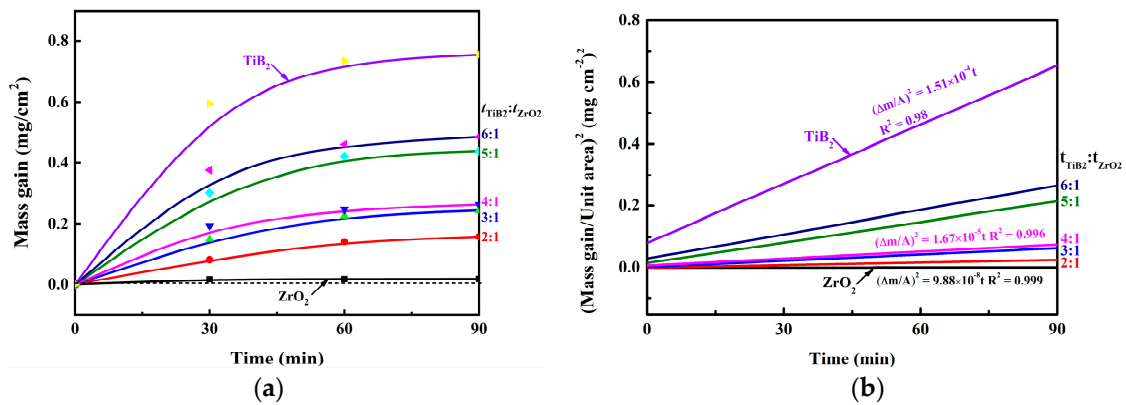
Figure 6. (**a**) The thermogravimetric curves and (**b**) the plots of $(\Delta m/A)^2$ versus time of the TiB_2 and ZrO_2 monolayers and the TiB_2/ZrO_2 multilayers during oxidation.

The parabolic oxidation rate can be expressed by Equation (2):

$$\left(\frac{\Delta m}{A}\right)^2 = kt + c \tag{2}$$

where t is the time, Δm is the mass change, A is the surface area of the sample, k is the parabolic rate constant, and c is a constant.

Figure 6b shows plots of $(\Delta m/A)^2$ vs. t with linear fits to the data. Evidently, the data points can be fitted to straight lines. All curves obey the parabolic law, indicating that the oxidation reaction was controlled by diffusion. The coefficients of determination (R^2) were in the range of 0.98–0.99, indicating that the data were well fit by straight lines. The values of k are shown in Table 1. The activation energies of the multilayers were calculated using the Arrhenius equation (Equation (3)):

$$k = A_0 \exp\left(\frac{E_a}{RT}\right) \tag{3}$$

where T is the absolute temperature, R is the gas constant, A_0 is the pre-exponential constant, and E_a is the activation energy, which can be calculated from Equation (4):

$$\text{In}k = \text{In}A_0 - \frac{E_a}{RT} \tag{4}$$

Table 1. The calculated K, R^2 and E_a (activation energy) values of TiB_2, ZrO_2 monolayers and TiB_2/ZrO_2 multilayers tested at 600 °C, respectively.

Coating Style	Absolute Temperature (K)	K (mg^2 cm^{-4} t^{-1})	R^2 (Correlation Coefficient)	E_a (KJ mol^{-1})
ZrO_2	873.15	9.88×10^{-8}	0.99	140.87
$t_{TiB_2}:t_{ZrO_2}$ =2:1	873.15	4.58×10^{-6}	0.99	107.34
$t_{TiB_2}:t_{ZrO_2}$ =3:1	873.15	1.25×10^{-5}	0.99	98.60
$t_{TiB_2}:t_{ZrO_2}$ =4:1	873.15	1.67×10^{-5}	0.99	96.07
$t_{TiB_2}:t_{ZrO_2}$ =5:1	873.15	4.52×10^{-5}	0.99	87.34
$t_{TiB_2}:t_{ZrO_2}$ =6:1	873.15	6.05×10^{-5}	0.98	84.83
TiB_2	873.15	1.51×10^{-5}	0.98	76.84

Table 1 shows the E_a values for the oxidation of the TiB_2 and ZrO_2 monolayers and the TiB_2/ZrO_2 multilayers. The E_a values for the oxidation of the TiB_2 and ZrO_2 monolayers were approximately 76.84 and 140.87 kJ/mol, respectively, indicating that the ZrO_2 monolayers were less likely to react with oxygen compared to the TiB_2 monolayers under the same conditions. For the multilayers, E_a decreased

with increasing modulation ratio, and the E_a values were higher than that of the TiB$_2$ monolayer. Discontinuous oxidation retarded the inward diffusion of oxygen and hindered the outward diffusion of metallic components. The formation of a dense (Ti, B)-oxide scale and the internally inserted ZrO$_2$ layers in the TiB$_2$/ZrO$_2$ multilayers enhanced the oxidation resistance of the multilayers [7,38].

To verify the synergetic enhancement of the oxidation resistance and mechanical properties, the hardness, residual stress (Figure 7a), and elastic modulus (Figure 7b) of the TiB$_2$ and ZrO$_2$ monolayers and the TiB$_2$/ZrO$_2$ multilayers were measured before and after annealing. The higher TiB$_2$ fraction with increasing ratio from 2:1 to 6:1 the hardness increased. It almost followed the rule of mixture of the individual components [39] Herein, with increasing t_{TiB_2}:t_{ZrO_2}, the hardness and elastic modulus both improved, reaching their highest values of 23.9 GPa and 303.1 GPa before annealing. Accordingly, Figure 7b shows a decrease in hardness and elastic modulus after oxidation. The hardness reduction during oxidation was basically due to the decreasing fraction of TiB$_2$. The reduction in residual stress also caused by high-temperature oxidation results in reduced hardness [40]. After annealing at 600 °C, the hardness of the oxidized multilayers did not increase as the oxidation resistance of the multilayers did. Instead, a critical point appears at t_{TiB_2}:t_{ZrO_2} = 4:1, where both the hardness and elastic modulus reach their maximum values of approximately 16.4 GPa and 262.4 GPa. These values are much higher than those of the TiB$_2$ monolayers. In addition, among the multilayers, annealing resulted in the smallest reductions in hardness and elastic modulus for the multilayer with t_{TiB_2}:t_{ZrO_2} = 4:1 (Figure 7b).
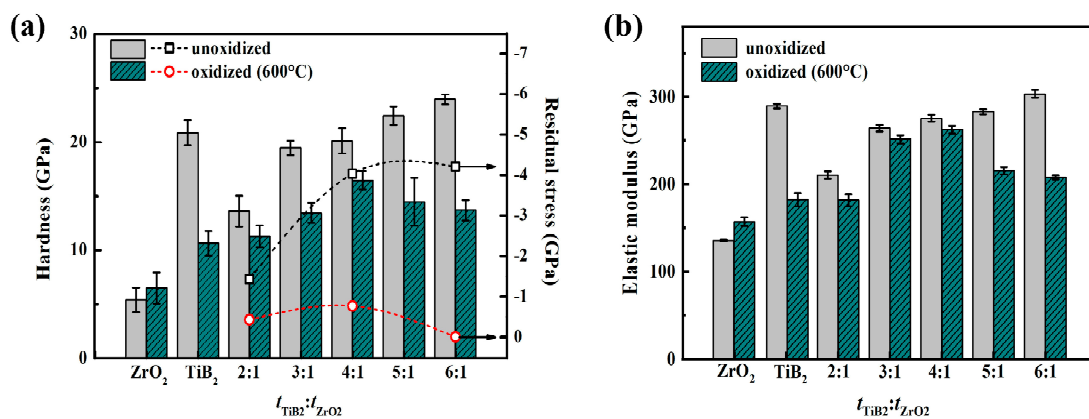

Figure 7. The hardnes, residual stress (**a**), and elastic modulus (**b**) of the TiB$_2$ and ZrO$_2$ monolayers and the TiB$_2$/ZrO$_2$ multilayers with different t_{TiB_2}:t_{ZrO_2} before and after annealing.

Figure 8 shows the results of scratch scan and post scan surface profiles of TiB$_2$ monolayers and TiB$_2$/ZrO$_2$ (t_{TiB_2}:t_{ZrO_2} = 4:1) multilayers before and after annealing. The maximum load was 5 N. The critical fracture load can be used to characterize the adhesion strength or fracture resistance of the coating. The loads of first cracking for the TiB$_2$ monolayers and TiB$_2$/ZrO$_2$ (t_{TiB_2}:t_{ZrO_2} = 4:1) multilayers before annealing were 4.17 and 4.02 N, respectively. Meanwhile, only slight cracks were observed at the edges of the coatings, and they did not delaminate with the tracks, indicating the good strengths of the TiB$_2$ monolayers and TiB$_2$/ZrO$_2$ (t_{TiB_2}:t_{ZrO_2} = 4:1) multilayers on the substrates. Owing to the formation of oxidation products and the oxidation of the interface to the substrate itself, the critical fracture load of TiB$_2$/ZrO$_2$ (t_{TiB_2}:t_{ZrO_2} = 4:1) multilayers (3.91 N) was higher than the TiB$_2$ monolayers (3.14 N) after annealing, and the fracture range was smaller. This indicated that the TiB$_2$/ZrO$_2$ (t_{TiB_2}:t_{ZrO_2} = 4:1) multilayers enhances the adhesion strength with the substrate and is in favor of releasing the residual stress.

Our experimental observations showed that the oxidation resistance of the multilayers increased as the modulation ratio decreased. That is, as the ZrO$_2$ layers became thicker, the progressive oxidation of the multilayers from top to bottom became more difficult. The change in hardness with annealing was studied based on the proposed oxidation mechanism, which takes into account changes in the mechanical properties of the layers due to oxidation and the development of internal stresses to

accommodate the volume increase associated with the oxidation of multilayers during annealing. The hardness of the annealed multilayers should also increase as the modulation ratio decrease. The experimental results did not indicate a further increase in hardness for the multilayers with $t_{TiB_2}:t_{ZrO_2} = 4:1$. This behavior was associated with the development of damage at the interfaces between the ZrO_2 and TiB_2 layers, and the corresponding rule of mixtures for composites. The construction of the multilayer system with controlled ZrO_2 content provided a multilayer structure with good oxidation resistance while maintaining a high hardness.
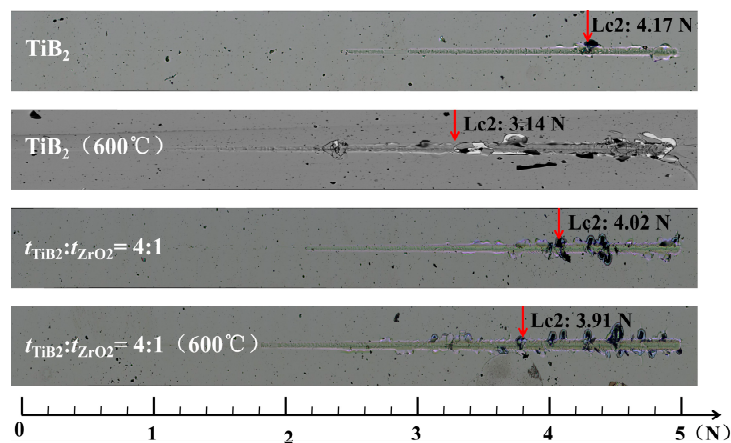

Figure 8. Scratch track images of TiB_2 monolayers and TiB_2/ZrO_2 ($t_{TiB_2}:t_{ZrO_2} = 4:1$) multilayers before and after annealing.

4. Conclusions

In this work, TiB_2/ZrO_2 multilayers with a constant modulation period along with TiB_2 and ZrO_2 monolayers for comparison were synthesized on Si (100) substrates by magnetron sputtering. The oxidation behaviors of the samples upon annealing at 600 °C were investigated. The deposited multilayers were dense and maintained their periodic structures after annealing. The oxidation resistance and mechanical properties of the multilayers before and after high-temperature oxidation were studied based on an oxidation mechanism model. The TiB_2/ZrO_2 multilayers exhibited a significantly higher E_a for oxidation (~107.34 kJ/mol) than TiB_2 monolayer (~76.84 kJ/mol). The maximum hardness (16.4 GPa) and elastic modulus (262.4 GPa) of the oxidized multilayers were observed at $t_{TiB_2}:t_{ZrO_2} = 4:1$. The superior mechanical properties and oxidation resistance of the TiB_2/ZrO_2 multilayers were attributed to the synergistic contributions of the modulated thickness of the TiB_2 and ZrO_2 layers and the discontinuous oxidation of the multilayers. The findings of this work demonstrate that ceramics/metal oxide nanocomposites with enhanced oxidation resistance and mechanical properties can be obtained via structural optimization.

References

1. Monclus, M.A.; Callisti, M.; Polcar, T.; Yang, L.W.; Llorca, J.; Molina-Aldareguia, J.M. Selective oxidation-induced strengthening of Zr/Nb nanoscale multilayers. *Acta Mater.* **2017**, *122*, 1–10. [CrossRef]

2. Cho, S.; Jo, I.; Lee, Y.-H.; Yoo, Y.W.; Byon, E.; Lee, S.-K.; Lee, S.-B. Highly improved oxidation resistance of TiC-SKD11 composite by SiC/TiB$_2$ based hybrid coating. *Appl. Surf. Sci.* **2018**, *448*, 407–415. [CrossRef]

3. Shimada, S.; Takahashi, M.; Kiyono, H.; Tsujino, J. Coatings and microstructures of monolithic TiB$_2$ films and double layer and composite TiCN/TiB$_2$ films from alkoxide solutions by thermal plasma CVD. *Thin Solid Films* **2008**, *516*, 6616–6621. [CrossRef]

4. Ma, A.; Jiang, M. The Study on oxidative dynamic of TiB$_2$ ceramic. *Ceramics* **2006**, *7*, 19–21. (In Chinese) [CrossRef]

5. Mokhayer, M.M.; Kakroudi, M.G.; Milani, S.S.; Ghiasi, H.; Vafa, N.P. Investigation of AlN addition on the microstructure and mechanical properties of TiB$_2$ ceramics. *Ceram. Int.* **2019**, *45*, 16577–16583. [CrossRef]

6. Zhirkov, I.; Petruhins, A.; Naslund, L.-A.; Kolozsvári, S.; Polcik, P.; Rosen, J. Vacuum arc plasma generation and thin film deposition from a TiB$_2$ cathode. *Appl. Phys. Lett.* **2015**, *107*, 184103. [CrossRef]

7. Li, H.; Sun, Y.; Zhang, J. Effect of ZrO$_2$ particle on the performance of micro-arc oxidation coatings on Ti6Al4V. *Appl. Surf. Sci.* **2015**, *342*, 183–190. [CrossRef]

8. Moon, J.; Choi, H.; Kim, H.; Lee, C. The effects of heat treatment on the phase transformation behavior of plasma-sprayed stabilized ZrO$_2$ coatings. *Surf. Coat. Technol.* **2002**, *155*, 1–10. [CrossRef]

9. Mahnicka-Goremikina, L.; Svinka, R.; Svinka, V. Influence of ZrO$_2$ and WO$_3$ doping additives on the thermal properties of porous mullite ceramics. *Ceram. Int.* **2018**, *44*, 16873–16879. [CrossRef]

10. Li, Y.; Li, J.; Liang, R.; Zhao, R.; Xiong, B.; Liu, H.; Tian, H.; Yang, Y.; Ren, T.-L. Switching dynamics of ferroelectric HfO$_2$–ZrO$_2$ with various ZrO$_2$ contents. *Appl. Phys. Lett.* **2019**, *114*, 142902. [CrossRef]

11. Ramana, C.V.; Vemuri, R.S.; Fernandez, I.; Campbell, A.L. Size-effects on the optical properties of zirconium oxide thin films. *Appl. Phys. Lett.* **2009**, *95*, 231905. [CrossRef]

12. Yao, J.; He, Y.; Wang, D.; Lin, J. High-temperature oxidation resistance of (Al$_2$O$_3$–Y$_2$O$_3$)/(Y$_2$O$_3$-stabilized ZrO$_2$) laminated coating on 8Nb–TiAl alloy prepared by a novel spray pyrolysis. *Corrosion Sci.* **2014**, *80*, 19–27. [CrossRef]

13. Guo, C.; Zhou, J.; Chen, J.; Zhao, J.; Yu, Y.; Zhou, H. Improvement of the oxidation and wear resistance of pure Ti by laser cladding at elevated temperature. *Surf. Coat. Technol.* **2010**, *205*, 2142–2151. [CrossRef]

14. Ryabchikov, A.I.; Kashkarov, E.B.; Pushilina, N.S.; Syrtanov, M.S.; Shevelev, A.E.; Korneva, O.S.; Sutygina, A.N.; Lider, A.M. High-intensity low energy titanium ion implantation into zirconium alloy. *Appl. Surf. Sci.* **2018**, *439*, 106–112. [CrossRef]

15. Wu, H.; Zhang, P.; Zhao, H.; Wang, L.; Xie, A. Effect of different alloyed layers on the high temperature oxidation behavior of newly developed Ti$_2$AlNb-based alloys. *Appl. Surf. Sci.* **2011**, *257*, 1835–1839. [CrossRef]

16. Li, G.; Li, Y.; Li, G. Coherent growth and superhardness effect in VC/Si$_3$N$_4$ nanomultilayers. *Surf. Coat. Technol.* **2011**, *205*, 3881–3884. [CrossRef]

17. Fu, T.; Zhang, Z.; Peng, X.; Weng, S.; Miao, Y.; Zhao, Y.; Fu, S.; Hu, N. Effects of modulation periods on mechanical properties of V/VN nano-multilayers. *Ceram. Int.* **2019**, *45*, 10295–10303. [CrossRef]

18. Yin, D.; Peng, X.; Qin, Y.; Wang, Z. Template effect in TiN/AlN multilayered coatings from first principles. *Ceram. Int.* **2015**, *41*, 10095–10101. [CrossRef]

19. Shah, S.A.; Khan, A.F.; Khan, A.; Rahim, N.A.; Mehmood, M. Multilayer Si/Ge thin films with quantum confinement effects for photovoltaic applications. *Appl. Surf. Sci.* **2014**, *296*, 185–188. [CrossRef]

20. Yang, F.J.; Wang, H.; Wang, H.B.; Cao, X.; Li, Q.; Zhou, M.J. Effect of interfacial diffusion on microstructure and properties of FePt/B$_4$C multifunctional multilayer composite films. *Appl. Surf. Sci.* **2008**, *254*, 2516–2520. [CrossRef]

21. Pan, Y.; Lei, D.; Na, L.; Yu, J.; Li, C.; Li, D. Investigating the influence of epitaxial modulation on the evolution of superhardness of the VN/TiB$_2$ multilayers. *Appl. Surf. Sci.* **2016**, *390*, 406–411. [CrossRef]

22. Junhua, X.; Geyang, L.; Mingyuan, G. The microstructure and mechanical properties of TaN/TiN and TaWN/TiN superlattice films. *Thin Solid Films* **2000**, *370*, 45–49. [CrossRef]

23. Saladukhin, I.A.; Abadias, G.; Uglov, V.V.; Zlotski, S.V.; Michel, A.; Janse van Vuuren, A. Thermal stability and oxidation resistance of ZrSiN nanocomposite and ZrN/SiN$_x$ multilayered coatings: A comparative study. *Surf. Coat. Technol.* **2017**, *332*, 428–439. [CrossRef]

24. Yao, X.; Li, H.; Zhang, Y.; Ren, J.; Yao, D.; Tao, J. A SiC/ZrB$_2$–SiC/SiC oxidation resistance multilayer coating for carbon/carbon composites. *Corrosion Sci.* **2012**, *57*, 148–153. [CrossRef]

25. Lei, Z.; Liu, Y.; Fei, M.; Song, Z.; Li, Y. Oxidation resistance of TiAlN/ZrN multilayer coatings. *Vacuum* **2016**, *127*, 22–29. [CrossRef]

26. Janssen, G.C.A.M.; Abdalla, M.M.; van Keulen, F.; Pujada, B.R.; van Venrooy, B. Celebrating the 100th anniversary of the Stoney equation for film stress: developments from polycrystalline steel strips to single crystal silicon wafers. *Thin Solid Films* **2009**, *517*, 1858–1867. [CrossRef]

27. Legoues, F.K.; Mooney, P.M.; Tersoff, J. Measurement of the activation barrier to nucleation of dislocations in thin films. *Phys. Rev. Lett.* **1993**, *71*, 396–399. [CrossRef] [PubMed]

28. Xu, X.; Sheng, X.L.; Zhang, T.F.; Liu, M.; Xin, X.L. Raman spectrum and friction behaviors of carbon-doped TiB$_2$ films prepared by magnetron sputtering. *J. Mater. Eng.* **2012**, *2*, 30–32. [CrossRef]

29. Bondarev, A.V.; Kiryukhantsev-Korneev, P.V.; Levashov, E.A.; Shtansky, D.V. Tribological behavior and self-healing functionality of TiNbCN–Ag coatings in wide temperature range. *Appl. Surf. Sci.* **2017**, *396*, 110–120. [CrossRef]

30. Maniu, D.; Iliescu, T.; Ardelean, I.; Cinta-Pinzaru, S.; Tarcea, N.; Kiefer, W. Raman study on B$_2$O$_3$–CaO glasses. *J. Mol. Struct.* **2003**, *651–653*, 485–488. [CrossRef]

31. Song, Y.; Zheng, X.; Yu, G.; Zhao, J.; Jiang, L.; Liu, Y.; Yang, B.; Yang, Y. The characteristics of laser-driven shock wave investigated by time-resolved Raman spectroscopy. *J. Raman Spectrosc.* **2011**, *42*, 345–348. [CrossRef]

32. Tampieri, A.; Bellosi, A. Oxidation of monolithic TiB$_2$ and of Al$_2$O$_3$−TiB$_2$composite. *J. Mater. Sci.* **1993**, *28*, 649–653. [CrossRef]

33. Tao, G.; He, J.; Pang, X.; Volinsky, A.A.; Su, Y.; Qiao, L. High temperature brittle film adhesion measured from annealing-induced circular blisters. *Acta Mater.* **2017**, *138*, 1–9. [CrossRef]

34. Liang, B.; Chen, H. Overview of the application and development of ZrO$_2$ coatings (films). *Bull. Chin. Ceram. Soc.* **2003**. (In Chinese) [CrossRef]

35. Dang, C.; Li, J.; Wang, Y.; Chen, J. Structure, mechanical and tribological properties of self-toughening TiSiN/Ag multilayer coatings on Ti6Al4V prepared by arc ion plating. *Appl. Surf. Sci.* **2016**, *386*, 224–233. [CrossRef]

36. Xiao, B.; Li, H.; Mei, H.; Dai, W.; Zuo, F.; Wu, Z.; Wang, Q. A study of oxidation behavior of AlTiN- and AlCrN-based multilayer coatings. *Surf. Coat. Technol.* **2018**, *333*, 229–237. [CrossRef]

37. Xu, Y.X.; Riedl, H.; Holec, D.; Li, C.; Yong, D.; Mayrhofer, P.H. Thermal stability and oxidation resistance of sputtered Ti−Al−Cr−N hard coatings. *Surf. Coat. Technol.* **2017**, *324*, 48–56. [CrossRef]

38. Dong, K.F.; Li, H.H.; Peng, Y.G.; Ju, G.; Chow, G.M.; Chen, J.S. L1$_0$FePt−ZrO$_2$ (001) nanostructured films with high aspect ratio columnar grains. *Appl. Phys. Lett.* **2014**, *104*, 192404. [CrossRef]

39. Sarkar, B.K.; Mukherjee, M.K.; Natarajan, A. A modification of the rule of mixture in estimating strengths of a composite. *Mater. Sci. Eng. Technol.* **1982**, *13*, 269–273. [CrossRef]

40. Bouaouina, B.; Besnard, A.; Abaidia, S.E.; Haid, F. Residual stress, mechanical and microstructure properties of multilayer Mo$_2$N/CrN coating produced by R.F Magnetron discharge. *Appl. Surf. Sci.* **2017**, *395*, 117–121. [CrossRef]